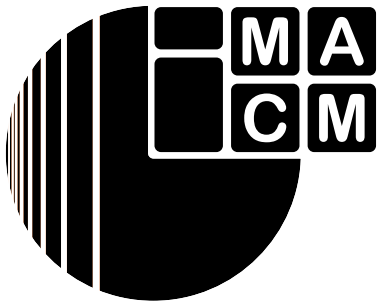

Bergische Universität Wuppertal

Fachbereich Mathematik und Naturwissenschaften

Institute of Mathematical Modelling, Analysis and Computational Mathematics (IMACM)

Preprint BUW-IMACM 17/16

G. Tauzin, L. Biferale, M. Sbragaglia, A. Gupta, F. Toschi,
A. Bartel and M. Ehrhardt

A numerical tool for the study of the hydrodynamic recovery of the Lattice Boltzmann Method

December 2017

http://www.math.uni-wuppertal.de

A numerical tool for the study of the hydrodynamic recovery of the Lattice Boltzmann Method

Guillaume Tauzin[a,c,*], Luca Biferale[a], Mauro Sbragaglia[a], Abhineet Gupta[b], Federico Toschi[b], Andreas Bartel[c], Matthias Ehrhardt[c]

[a]*Dipartimento di Fisica and INFN, Università di Roma "Tor Vergata", Via della Ricerca Scientifica 1, 00133 Roma, Italy*
[b]*Department of Applied Physics and Department of Mathematics and Computer Science, Eindhoven University of Technology, 5612 AZ Eindhoven, Netherlands*
[c]*Chair of Applied Mathematics and Numerical Analysis, Bergische Universität Wuppertal, Gaußstrasse 20, 42119 Wuppertal, Germany*

Abstract

We investigate scale-by-scale the hydrodynamic recovery of Lattice Boltzmann Method (LBM) simulations. To this aim, we introduce a new tool based on the systematic evaluation of each term of the kinetic energy and enstrophy balance equations averaged over randomly selected sub-volumes of the computational domain. In the context of 2D isotropic homogeneous turbulence, we first validate this approach on decaying turbulence by comparing the hydrodynamic recovery of an ensemble of LBM simulations against the one of an ensemble of Pseudo-Spectral (PS) simulations. We then conduct a benchmark of LBM simulations of forced turbulence with increasing Reynolds number by varying the input relaxation times of LBM. This approach can be extended to the study of implicit sub-grid scale (SGS) models, thus offering a promising route to quantify the implicit SGS models implied by existing stabilization techniques within the LBM framework.

Keywords: Lattice Boltzmann Method, Hydrodynamics, Turbulence modeling

1. Introduction

The simulation of turbulent flows pertains to a vast diversity of applications in engineering [1]. The high Reynolds number associated with the phenomenon of turbulence requires solving a wide

*Corresponding author:
Email address: guillaume.tauzin@roma2.infn.it (Guillaume Tauzin)

range of scales on a high resolution computational grid, making their Direct Numerical Simulation (DNS) typically out of reach [2, 3]. Large-Eddy Simulation (LES) is a workaround which allows a reduction of the number of degrees of freedom. LES is acknowledged in the engineering community as a cost-effective alternative to DNS [4, 5, 6]. The principle of LES is to solve flow scales up to a cut-off and to filter the small scales out. As large scales and smaller scales are coupled, unresolved small scales need to be modeled using a so-called sub-grid scale (SGS) model. A large number of filtering techniques and SGS models have been proposed in the Navier-Stokes framework [7].

The Lattice Boltzmann Method (LBM) is a meso-scale flow solver that has been gaining popularity because of its intrinsic scalability, as well as its ability to deal with multiple physics and complex boundary conditions [8, 9, 10]. The LBM equation describes the streaming and collision of distribution functions $f_\ell(\vec{x}, t)$ on a lattice with a finite set of kinetic velocities $\vec{c}_\ell,\ \ell = 0 \dots q-1$. The collision operator is popularly modeled by the Bhatnagar-Gross-Krook (BGK) [11] relaxation towards a local equilibrium with a dimensionless relaxation time τ

$$f_\ell(\vec{x} + \vec{c}_\ell \Delta t, t + \Delta t) - f_\ell(\vec{x}, t) = -\frac{1}{\tau}\left[f_\ell(\vec{x}, t) - f_\ell^{eq}(\vec{x}, t)\right] + F_\ell \tag{1}$$

where F_ℓ is a suitable forcing term designed to reproduce a macroscopic forcing [8, 9, 10]. From a theoretical point of view, the use of a multi-scale Chapman-Enskog (CE) perturbative expansion allows to recover hydrodynamic equations. In brief, one expands the distribution function in a power-series: $f_\ell = f_\ell^{(eq)} + K_n f_\ell^{(1)} + K_n^2 f_\ell^{(2)} + ...$, where $K_n = \lambda/L \ll 1$ is the Knudsen number, giving the ratio between the particles mean free path λ and the macroscopic scale L. Furthermore, space and time are rescaled, *i.e.* $\vec{x}^{(1)} = K_n \vec{x}$, $t^{(1)} = K_n t$, $t^{(2)} = K_n^2 t$ by introducing separate time scales for the effect of advection ($t^{(1)}$) and dissipation ($t^{(2)}$) [8, 9]. Performing this procedure for a local equilibrium distribution chosen as (repeated indices are meant summed upon)

$$f_\ell^{eq}(\vec{x},\, t) = f_\ell^{eq}\left(\rho(\vec{x},\, t),\, \vec{u}(\vec{x},\, t)\right) = t_\ell\, \rho \left[1 + \frac{c_{\ell,i} u_i}{c_s^2} + \frac{\left(c_{\ell,i} u_i\right)^2}{2c_s^4} - \frac{u_i u_i}{2c_s^2}\right], \tag{2}$$

where t_ℓ is a set of lattice-dependent weighting factors and c_s the speed of sound in the lattice, one can recover the athermal weekly compressible Navier-Stokes hydrodynamic equations for the density field $\rho(\vec{x},\, t) = \sum_{\ell=0}^{q-1} f_\ell(\vec{x},\, t)$ and velocity field $\vec{u}(\vec{x},\, t) = \sum_{\ell=0}^{q-1} f_i(\vec{x},\, t)\, \vec{c}_\ell / \rho(\vec{x},\, t)$

$$\partial_t \rho + \partial_j(\rho u_j) = 0 + O(K_n^2) \tag{3}$$

$$\partial_t(\rho u_i) + \partial_j\left(\rho u_i u_j\right) = -\partial_i p + \partial_j\left(\rho\nu\left(\partial_j u_i + \partial_i u_j\right)\right) + F_i + O(K_n^2) + O(M_a^3). \tag{4}$$

Beyond the higher order corrections in the Knudsen number, in the recovery of the momentum equations one usually neglects terms which are cubic in the velocity [12], hence we find the term $O(M_a^3)$, where the Mach number $M_a = \frac{U_{RMS}}{c_s}$ represents the ratio of the root mean square (RMS) velocity c_s. The term $p = c_s^2\rho$ is the fluid pressure and the viscosity ν is linearly dependent on the relaxation time τ in (5) and vanishes as $\tau \to 0.5$:

$$\nu = c_s^2\left(\tau - \frac{1}{2}\right)\Delta t. \tag{5}$$

The LBM community has been keenly proposing Navier-Stokes inspired LES techniques to combine the intrinsic scalability of LBM with turbulence SGS models. The majority of them are eddy viscosities models implemented by locally modifying the relaxation time τ, i.e. assuming that Eq. (5) holds and that an effective relaxation time $\tau_{\text{eff}}(\vec{x}, t)$ results in an effective viscosity $\nu_{\text{eff}}(\vec{x}, t)$ [13, 14, 15, 16]. Malaspinas & Sagaut have shown that this method is only valid in the athermal weakly compressible limit and proposed a consistent eddy viscosity closure extension for compressible thermal flows [17]. Instabilities of the LBM with a BGK collision operator (LBGK) arising for an input relaxation time $\tau_0 \to 0.5$, *i.e.* for an input viscosity $\nu_0 \to 0$, along with the low Ma, which is required to remain in a good approximation of Navier-Stokes, significantly limit the range of Reynolds number reachable in practice. Some eddy viscosity methods have been shown to extend the range of stability to relaxation times $\tau_0 \to 0.5$, making it possible to simulate higher Reynolds number flows for a fixed grid resolution [18]. Stabilization of LBGK has been linked to the existence of an underlying Lyapunov functional in the form of a discrete Boltzmann H-functional [19]. Karlin *et al.* [20] introduced the Entropic Lattice Boltzmann (ELBM): an LBGK ensuring the monotonicity of a convex H-functional commonly chosen as

$$H(\mathbf{f}) = \sum_{\ell=0}^{q-1} f_\ell \log\left(\frac{f_\ell}{t_\ell}\right), \ \mathbf{f} = \{f_\ell\}_{\ell=0}^{q-1}. \tag{6}$$

To equip a LBGK with an H-theorem, ELBM implements a collisional process with an effective relaxation time $\tau_{\text{eff}} = \frac{2\tau_0}{\alpha}$ to a local equilibrium distribution $\mathbf{f^{eq}}$ defined as the extremum of the

H-functional under the constraints of mass and momentum conservation. The parameter α is calculated locally (in space and time) and has a non-linear dependency on the distribution functions f_ℓ. While the result is an unconditionally stable LBGK for $\tau_0 \rightarrow 0.5$ ($\nu_0 \rightarrow 0$), we are also left with a side-effect effective viscosity ν_{eff}. Unfortunately, the non-linear dependency of the effective relaxation time on the distribution functions does not allow this effective viscosity to be expressed in terms of macroscopic quantities and therefore the physics behind it remains hidden. In 2008, Malaspinas *et al.* [21] proposed an approximate formulation of the effective viscosity $\nu_{\text{eff}}(\vec{x}, t) = \nu_0 + \nu_t(\vec{x}, t)$ using CE expansion assuming $\alpha \approx 2$ ($\tau_{\text{eff}} \approx \tau_0$). The resulting turbulent viscosity ν_{t} is

$$\nu_{\text{t}} = -\frac{c_s^2}{3}\tau_0^2 \Delta t^2 \frac{S_{\theta\kappa} S_{\kappa\gamma} S_{\gamma\theta}}{S_{\lambda\mu} S_{\lambda\mu}} \propto \frac{Tr(S^3)}{Tr(S^2)} \tag{7}$$

where $S_{ij} = \frac{1}{2}(\partial_i u_j + \partial_j u_i)$ is the strain-rate tensor. The above formula suggests a similarity with the Smagorinsky SGS model [22] $\nu_{\text{t}} = C_{smago} \Delta x^2 \sqrt{S_{\theta\kappa} S_{\theta\kappa}} \propto \sqrt{Tr(S^2)}$ while allowing back-scatter as it can change sign.

In order to quantify the validity of the ELBM methodology as a LES turbulence SGS model, one needs to be able to evaluate and understand the physics it implies. Firstly, one needs to control the hydrodynamic recovery and determine the whole range of scales where the Navier-Stokes equations are well recovered [23]. This is an unquestionable prerequisite. Secondly, one needs to further study the sub-grid scale model implied by the ELBM. Based on this philosophy, in this paper we propose a tool to numerically evaluate the Navier-Stokes hydrodynamic recovery of fluid flow simulations in the context of isotropic homogeneous turbulence. This tool is based on the systematic calculation of each term of the kinetic energy and enstrophy balance equations averaged over a suitable ensemble of sub-volumes of the computational grid. We define an error to a perfect balancing and conduct a statistical analysis over sub-volumes of different sizes to understand how the hydrodynamics is being recovered across scales.

The paper is organized as follows: in section 2 we introduce the balance equations, their averaged counterparts over a sub-volume V and we define balancing errors as a measure of the hydrodynamic recovery; in section 3 we present the numerical set-up for the simulations of 2D isotropic homogeneous turbulence and for the scale-by-scale statistical analysis of the balancing errors; in

section 4 we present a validation of the tool by comparing the hydrodynamic recovery of an ensemble of LBGK simulations to an ensemble of Pseudo-Spectral (PS) simulations in the case of decaying flows; in section 5 we benchmark the tool on LBGK simulations of forced turbulence for a range of decreasing input relaxation times τ_0, while linking the results to statistics of the Mach number across scales; some concluding remarks will follow in section 6.

2. Hydrodynamic recovery for energy and enstrophy balance in 2D

In order to characterize the hydrodynamic recovery of a simulation, we calculate the average over sub-volumes of the terms in both the kinetic energy and the enstrophy balance equations. Starting from the formulation of the macroscopic LBM momentum conservation (see Eq. (4)) and mass conservation (see Eq. (3)), one can obtain the kinetic energy ($E = \frac{\rho u_i u_i}{2}$) balance equation and the enstrophy ($\Omega = \frac{\omega_i \omega_i}{2}$, with ω_i the component of the vorticity $\vec{\omega} = \vec{\nabla} \times \vec{u}$ along $\vec{e}_i$) balance equation

$$\begin{aligned}\partial_t\left(\frac{\rho u_i u_i}{2}\right) =& - u_i \partial_i p - \nu\rho\left(\partial_j u_i + \partial_i u_j\right)\partial_j u_i + u_i F_i \\ & - \partial_j\left(\frac{\rho u_i u_i}{2} u_j\right) + \partial_j\left(\nu\rho u_i\left(\partial_j u_i + \partial_i u_j\right)\right)\end{aligned} \tag{8}$$

$$\begin{aligned}\partial_t\left(\frac{\omega_i\omega_i}{2}\right) =& - \partial_j\left(\frac{\omega_i\omega_i}{2}u_j\right) + \omega_i\omega_j\partial_j u_i + H_i(\nu)\epsilon_{ijk}\partial_j\omega_k + \omega_i\epsilon_{ijk}\partial_j\left(\frac{1}{\rho}F_k\right) \\ & - \partial_j\left(\frac{\omega_i\omega_i}{2}u_j\right) + \partial_j\left(\epsilon_{ijk}\omega_i H_k(\nu)\right)\end{aligned} \tag{9}$$

where ϵ is the Levi-Civita symbol and $H_i(\nu) = \frac{1}{\rho}\partial_j \nu\rho\left(\partial_i u_j + \partial_j u_i\right)$. Equations (8) and (9) are locally valid. The next step is to calculate the average of each term of the balance equations over a sub-volume

$$\begin{aligned}LHS_V^E =& \partial_t\langle\frac{\rho u_i u_i}{2}\rangle_V \\ =& - \langle\partial_j\left(\frac{\rho u_i u_i}{2}u_j\right)\rangle_V - \langle u_i\partial_i p\rangle_V + \langle u_i F_i\rangle_V \\ & - \langle\nu\rho\left(\partial_j u_i + \partial_i u_j\right)\partial_j u_i\rangle_V + \langle\partial_j\left(\nu\rho u_i\left(\partial_j u_i + \partial_i u_j\right)\right)\rangle_V \\ =& RHS_V^{E,1} + RHS_V^{E,2} + RHS_V^{E,3} + RHS_V^{E,4} + RHS_V^{E,5} \\ =& RHS_V^E\end{aligned} \tag{10}$$

$$
\begin{aligned}
LHS_V^{\Omega} &= \partial_t \langle \frac{\omega_i \omega_i}{2} \rangle_V \\
&= -\langle \partial_j \left(\frac{\omega_i \omega_i}{2} u_j \right) \rangle_V - \langle \frac{\omega_i \omega_i}{2} \partial_j u_j \rangle_V + \langle \omega_i \epsilon_{ijk} \partial_j \left(\frac{1}{\rho} F_k \right) \rangle_V \\
&\quad + \langle H_i(\nu) \epsilon_{ijk} \partial_j \omega_k \rangle_V + \langle \partial_j \left(\epsilon_{ijk} \omega_i H_k(\nu) \right) \rangle_V + \langle \omega_i \omega_j \partial_j u_i \rangle_V \\
&= RHS_V^{\Omega,1} + RHS_V^{\Omega,2} + RHS_V^{\Omega,3} + RHS_V^{\Omega,4} + RHS_V^{\Omega,5} + RHS_V^{\Omega,6} \\
&= RHS_V^{\Omega}
\end{aligned}
\tag{11}
$$

where $\langle \cdots \rangle_V$ denotes the average over a generic volume V. Equations (10) and (11) describe the physical balance between the time derivative of the averaged energy and enstrophy ($LHS_V^{E,\Omega}$) and the right-hand side ($RHS_V^{E,\Omega}$) comprising all the physical contributions responsible for their evolution: the effect of compressibility, dissipation, input, and the transport and diffusive fluxes. It is worth pointing out that equations (10) and (11) remain valid for a viscosity changing in space and time $\nu = \nu_{\text{eff}}(\vec{x}, t) = \nu_0 + \nu_t(\vec{x}, t)$. Notice that in 3D, the enstrophy balance must include another additional term stemming from vortex stretching [3].

To measure the accuracy of the hydrodynamic recovery over a sub-volume V, we define a balancing error for the kinetic energy and enstrophy balance, δ_V^E and δ_V^{Ω} respectively. At a time t, $\delta_V^{E,\Omega}(t)$ is obtained by dividing the absolute difference between the $RHS_V^{E,\Omega}(t)$ and the $LHS_V^{E,\Omega}(t)$ terms by maximum of the absolute value of the terms on the right hand side, *i.e.*

$$
\delta_V^E(t) = \frac{\left| RHS_V^E(t) - LHS_V^E(t) \right|}{\max_i \left| RHS_V^{E,i}(t) \right|} \tag{12}
$$

and

$$
\delta_V^{\Omega}(t) = \frac{\left| RHS_V^{\Omega}(t) - LHS_V^{\Omega}(t) \right|}{\max_i \left| RHS_V^{\Omega,i}(t) \right|}. \tag{13}
$$

If for a sub-volume V at a time t the balance equations are perfectly respected on average, we must have $\delta_V^E(t) \equiv \delta_V^{\Omega}(t) \equiv 0$.

3. Numerical set-up for the statistical analysis of 2D homogeneous isotropic turbulence hydrodynamics

To validate this hydrodynamic recovery check tool, we apply it to configurations obtained from simulations conducted on a periodic two-dimensional 256×256 computational grid. Turbulence is

triggered by a homogeneous isotropic forcing with a constant phase ϕ on a shell of (dimensionless) wavenumbers $\vec{k}$ of magnitude from 5 to 7 given in a stream-function formulation

$$F_\Psi^T(\vec{x}) = F_0^T \sum_{5\leq\|\vec{k}\|\leq 7} \cos\left(\frac{2\,\pi}{256}\vec{k}\cdot\vec{x}+\phi\right). \tag{14}$$

The corresponding force is then obtained by taking

$$F_x^T = \partial_y F_\Psi^T \qquad \text{and} \qquad F_y^T = -\partial_x F_\Psi^T, \tag{15}$$

which ensures that it does not input any incompressibility in the system as $\vec{\nabla}\cdot\vec{F^T} \equiv 0$. We use this forcing to define a time scale $T_f = \sqrt{\frac{2\pi}{k_f F_0^T}}$, where k_f is taken equal to six. To have some control on the Mach number and limit the effect of the backward energy cascade, characteristic of 2D turbulence [25, 26], we introduce a spectral forcing to damp large-scale energy

$$\vec{F^R}(\vec{x},\,t) = -F_0^R \sum_{1\leq\|\vec{k}\|\leq 2} \vec{\hat{u}}(\vec{k},\,t)\, e^{\frac{2\pi}{256}\vec{k}\cdot\vec{x}} \tag{16}$$

where $\vec{\hat{u}}(\vec{k},\,t)$ is the Fourier transform of $\vec{u}(\vec{x},\,t)$. The forcing amplitudes are fixed for all simulations to $F_0^T = 0.0008$ and $F_0^R = 0.00001$. LBGK simulations are conducted on a 2D lattice with 9 discrete velocities, D2Q9 [8, 9, 10], on which forcings are implemented using the exact-difference method forcing scheme [24]. The sub-volume averaged terms are calculated offline based on the outputted configuration fields. A 1$^{\text{st}}$ order explicit Euler scheme is used to evaluate time derivatives, while a 2$^{\text{nd}}$ order centered scheme is applied for the space-derivatives, respectively

$$\left.\frac{\partial \mathbf{A}}{\partial t}\right|_{i,j}^{n} \sim \frac{A_{i,j}^{n+1}-A_{i,j}^{n}}{\Delta t} \qquad \text{and} \qquad \left.\frac{\partial \mathbf{A}}{\partial x}\right|_{i,j}^{n} \sim \frac{A_{i+1,j}^{n}-A_{i-1,j}^{n}}{2\,\Delta x} \quad \& \quad \left.\frac{\partial \mathbf{A}}{\partial y}\right|_{i,j}^{n} \sim \frac{A_{i,j+1}^{n}-A_{i,j-1}^{n}}{2\,\Delta y}. \tag{17}$$

Examples of the balancing of the terms of the energy and enstrophy equations are illustrated in Figs. 1 and 2 respectively. In both cases, the matching between the left-hand side ($LHS_V^{E,\Omega}$) and the right-hand side ($RHS_V^{E,\Omega}$) of the equations is excellent, with very small discrepancies observed when zooming in. Typically, the total $RHS_V^{E,\Omega}$ terms are the result of the sum of significantly higher amplitude terms. Eventually, the resulting balancing errors $\delta_V^{E,\Omega}$ is of the order $O(10^{-3})$ for the kinetic energy balancing and $O(10^{-2})$ for the enstrophy balancing, highlighting an excellent hydrodynamic recovery.

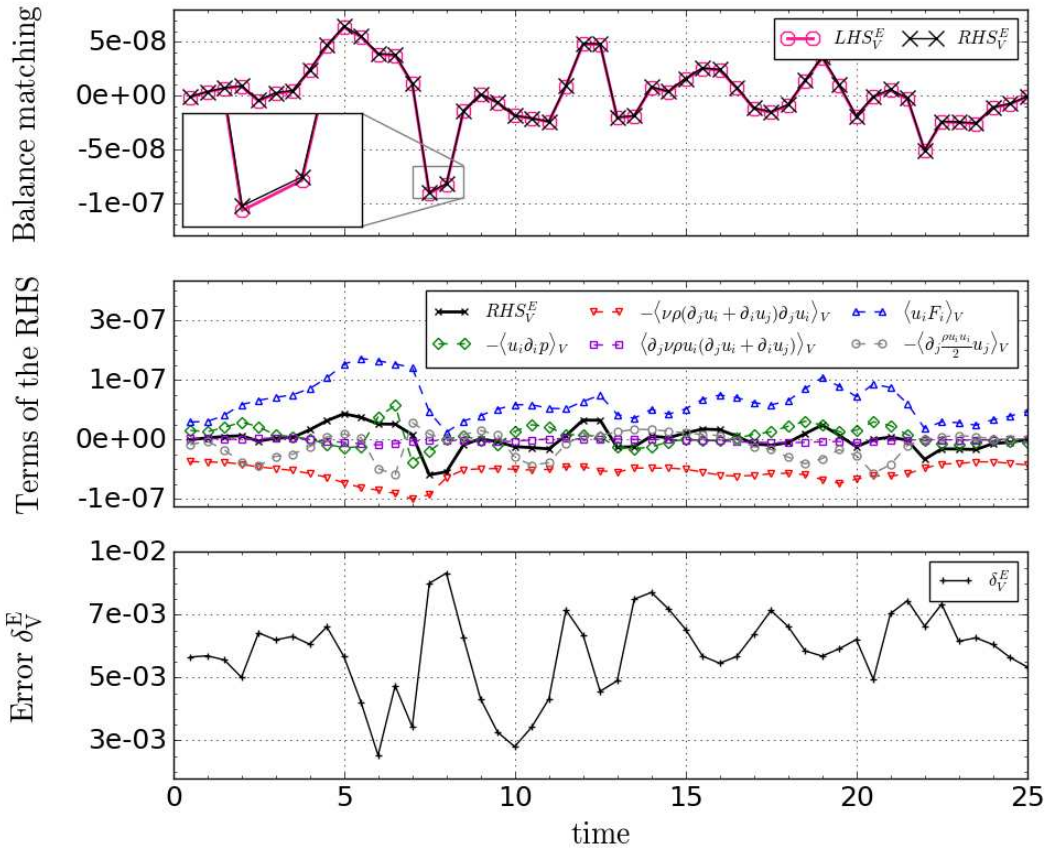

Figure 1: Typical time-evolution of the kinetic energy balancing over a single sub-volume of size 208×208 shown for a forced LBGK simulation with $\tau_0 = 0.55$ ($Re \approx 237$) on a 256×256 grid. The top figure shows the matching between the LHS_V^E and the RHS_V^E, the middle figure shows the contribution of each $RHS_V^{E,i}$ term and their sum RHS_V^E, and the bottom figure shows the balancing error δ_V^E.

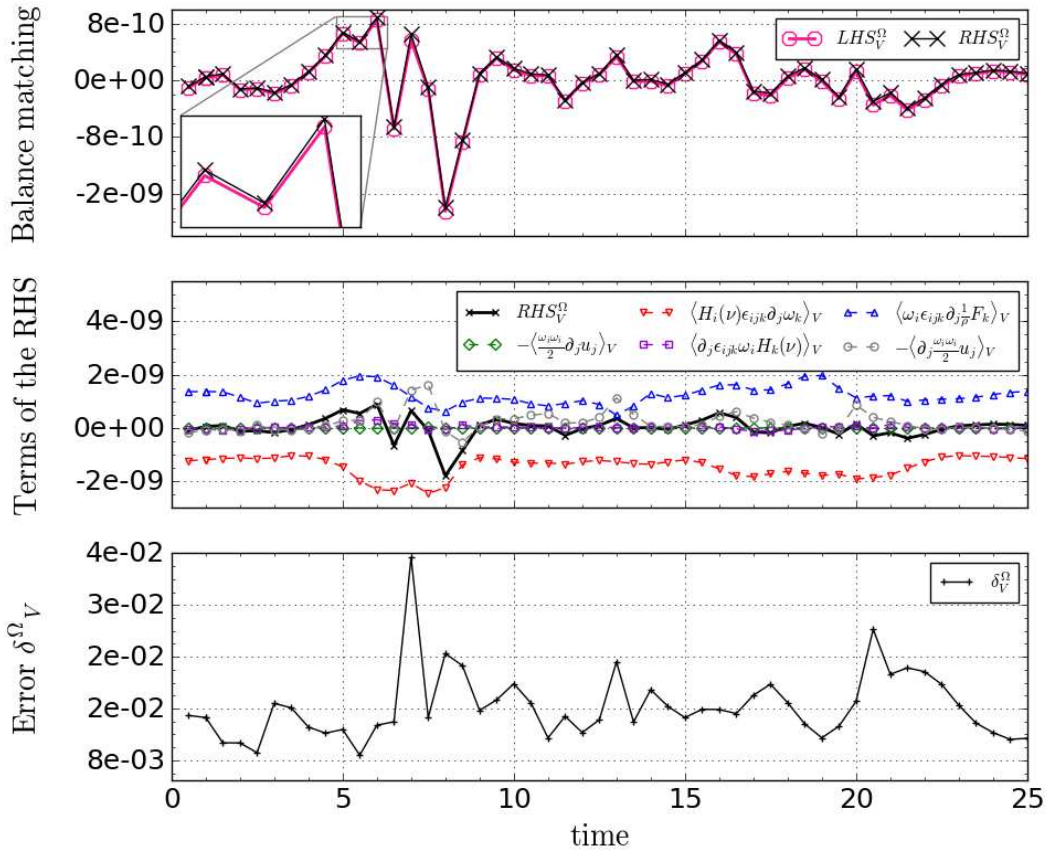

Figure 2: Typical time-evolution of the enstrophy balancing over a single sub-volume of size 208×208 shown for a forced LBGK simulation with $\tau_0 = 0.55$ ($Re \approx 237$) on a 256×256 grid. The top figure shows the matching between the LHS_V^Ω and the RHS_V^Ω, the middle figure shows the contribution of each $RHS_V^{\Omega,i}$ term and their sum RHS_V^Ω, and the bottom figure shows the balancing error δ_V^Ω.

In order to gather statistics of both balancing errors $\delta_V^{E,\Omega}(t)$ for a given scale L, we calculate them over squared sub-volumes $V = L \times L$ randomly chosen in space as illustrated in Fig. 3.

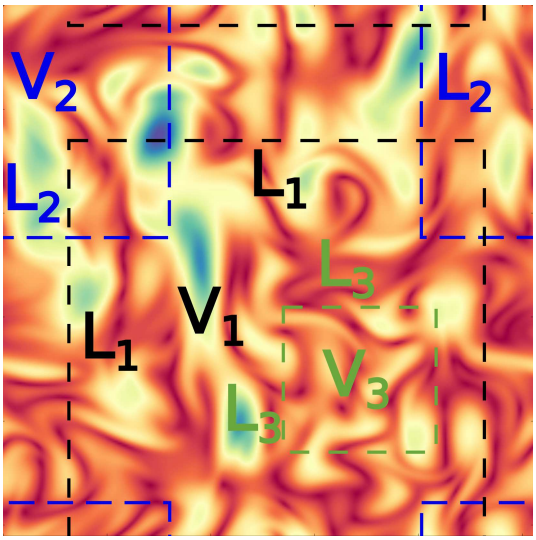

Figure 3: Illustration on a snapshot of the vorticity field of three random squared sub-volumes $V_1 = L_1 \times L_1$, $V_2 = L_2 \times L_2$, and $V_3 = L_3 \times L_3$ corresponding to the scales L_1, L_2, and L_3 respectively.

To present the results in terms of scales, we group together the balancing errors $\delta_L^{E,\Omega}(t) = \delta_{V=L\times L}^{E,\Omega}(t)$ obtained for all sub-volumes of the same scale L on the same configuration at time t. We conduct a statistical analysis and define their mean $\mu_L^{E,\Omega}(t)$ and their standard deviation $\sigma_L^{E,\Omega}(t)$. The number of sub-volumes processed for a scale L is shown in table 1.

Scale L	Number of sub-volumes processed
$L = 256$	1
$100 \leq L < 256$	5000
$10 \leq L < 100$	5000
$L < 10$	10000

Table 1: Number of sub-volumes processed for a scale L

4. Validation: LBGK against Pseudo-Spectral on an ensemble of decaying flow simulations

To understand how LBGK recovers hydrodynamics, we compare the statistics of the balancing errors obtained from LBGK simulations to the one obtained from PS simulations, which are used

as a reference. To this aim we generate ensembles of LBGK and PS simulations: we conduct a statistically stationary forced LBGK $\tau_0 = 0.52$ simulation that we sample into 25 configurations as shown in Fig. 4, the number 25 being chosen in order to recover smooth statistics. Each of those configurations is then used to restart both a LBGK simulation and a PS simulation at the same Reynolds number, thus ensuring that they solve the same physics. Specifically, we set

$$Re = \frac{U_{RMS}^{LBGK} L^{LBGK}}{\nu_0^{LBGK}} = \frac{U_{RMS}^{PS} L^{PS}}{\nu_0^{PS}} \tag{18}$$

with $U_{RMS}^{PS} = U_{RMS}^{LBGK} \frac{\Delta x^{LBGK}}{\Delta t^{LBGK}}$, $L^{PS} = 2\pi = L^{LBGK} \Delta x^{LBGK}$, and $\nu_0^{PS} = \nu_0^{LBGK} \frac{(\Delta x^{LBGK})^2}{\Delta t^{LBGK}}$ and where $\nu_0^{LBGK} = c_s^2(\tau_0 - 0.5)$ with $\tau_0 = 0.52$ in all simulations. Having fixed $\Delta x^{LBGK} = \frac{2\pi}{256}$, $\tau_0 = 0.52$, and $\Delta t^{LBGK} = 0.001$, we obtain $\nu_0^{PS} \approx 0.004$. We set $\Delta t^{PS} = 0.0005$ in order to be able to dump configurations of PS and LBGK simulations at the same physical time ($\Delta t^{LBGK} \propto \Delta t^{PS}$), while ensuring the stability of the PS simulations. Moreover, the velocity fields generated by the forced LBGK simulation have to be normalized by a factor $\frac{\Delta x^{LBGK}}{\Delta t^{LBGK}}$ before they are used to initialize the PS simulations. After initialization, the simulations are then left with no forcing to decay for a duration of $450\,T_f$, where T_f is the time scale based on the forcing as discussed in section 3. Eventually, the superposed ensemble-averaged energy spectrum for both ensemble at three selected times $t_1 = 0$, $t_2 = 225T_f$, and $t_3 = 450T_f$ are in very good agreement (Fig. 5). The pressure field for the PS simulations is obtained by solving, for each configuration, the Poisson equation for pressure, while the pressure field for the LBGK simulations is obtained directly from the density field $p = c_s^2 \rho$.

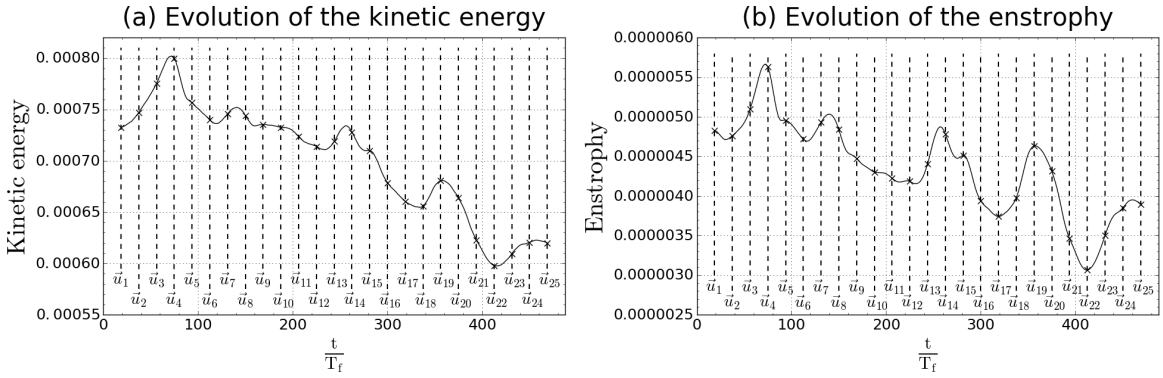

Figure 4: Evolution of the kinetic energy (a) and of the enstrophy (b) of the forced LBGK simulation. The 25 vertical lines highlight the sampled configurations used to initialize the 25 decaying flow simulations of the PS and the LBGK ensembles.

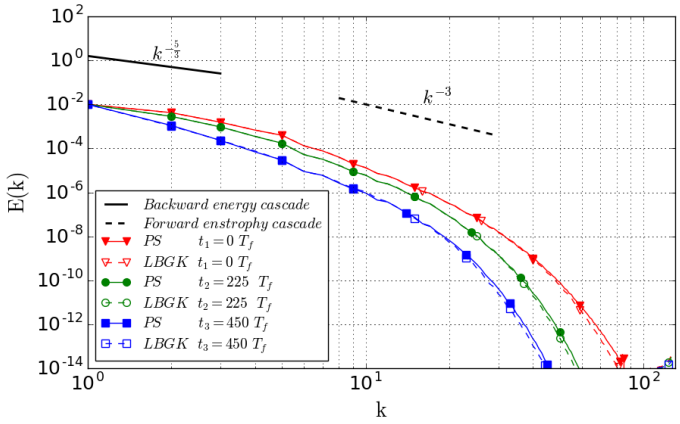

Figure 5: Superposed ensemble-averaged energy spectrum shown for three selected time instances for the PS and the LBGK simulations.

We show the results of the statistical analysis of the kinetic energy balancing error δ_L^E and enstrophy balancing error δ_L^Ω in Figs. 6 and 7 respectively. As expected, the PS method recovers hydrodynamics with a significant higher accuracy than the LBGK, with a clear improvement with time as the Reynolds number decreases and the simulations become increasingly resolved. This improvement with time can also be well appreciated in the LBGK simulations, especially in the analysis of the enstrophy balancing error in Fig. 7. Regarding the energy balancing error for LBGK in Fig. 6, the improvement with Reynolds number appears to be sub-leading, as both μ_L^E and σ_L^E

remain basically unchanged in time down to the scale $L \approx 8$. Below this threshold, it appears that inaccuracies in the balancing errors slightly increase with time. Taken all together, the statistical analysis of the balancing errors δ_L^E and δ_L^Ω show a strong non-local behavior, being an order of magnitude larger at small scales than at large scales (see dashed lines in Panels (c)-(d)).

To understand if the range of Mach numbers simulated affects the hydrodynamic recovery, we plot the statistics on the Mach number at scale L, *i.e.*

$$Ma_L = \langle \frac{U_{RMS}}{c_s} \rangle_{V=L\times L} \tag{19}$$

as shown in Fig. 8. We observe a steady mean (Fig. 8-(c)) going from about 0.55 to 0.4, and a steady standard deviation (Fig. 8-(d)) up to $L \approx 20$. As expected for decaying flows, the Mach number gradually decreases in time for all scales. The comparison between PS and LBGK is quite helpful to further assess the importance of the terms proportional to M_a^3 neglected in the momentum equation (see Eq. (4)). Indeed, if we look at the statistics of the enstrophy balancing errors δ_L^Ω in Fig. 7 for the first time $t = t_1$, we found that LBGK and PS are in very good agreement, meaning that the Mach number is low enough for the higher order terms in the LBGK macroscopic equation to be negligible. From the perspective of the statistics of the kinetic energy balancing error δ_L^E (see Fig. 6), we notice that if the Mach number was impacting the energy balancing error, we would have observed a statistics that varies in time as the Mach number decays. Overall, we can conclude that for the range of simulated Mach numbers the LBGK is a trustworthy Navier-Stokes solver, *i.e.* the Mach number is low enough so that all higher order Mach number terms that were neglected in the momentum equation do not affect the hydrodynamics.

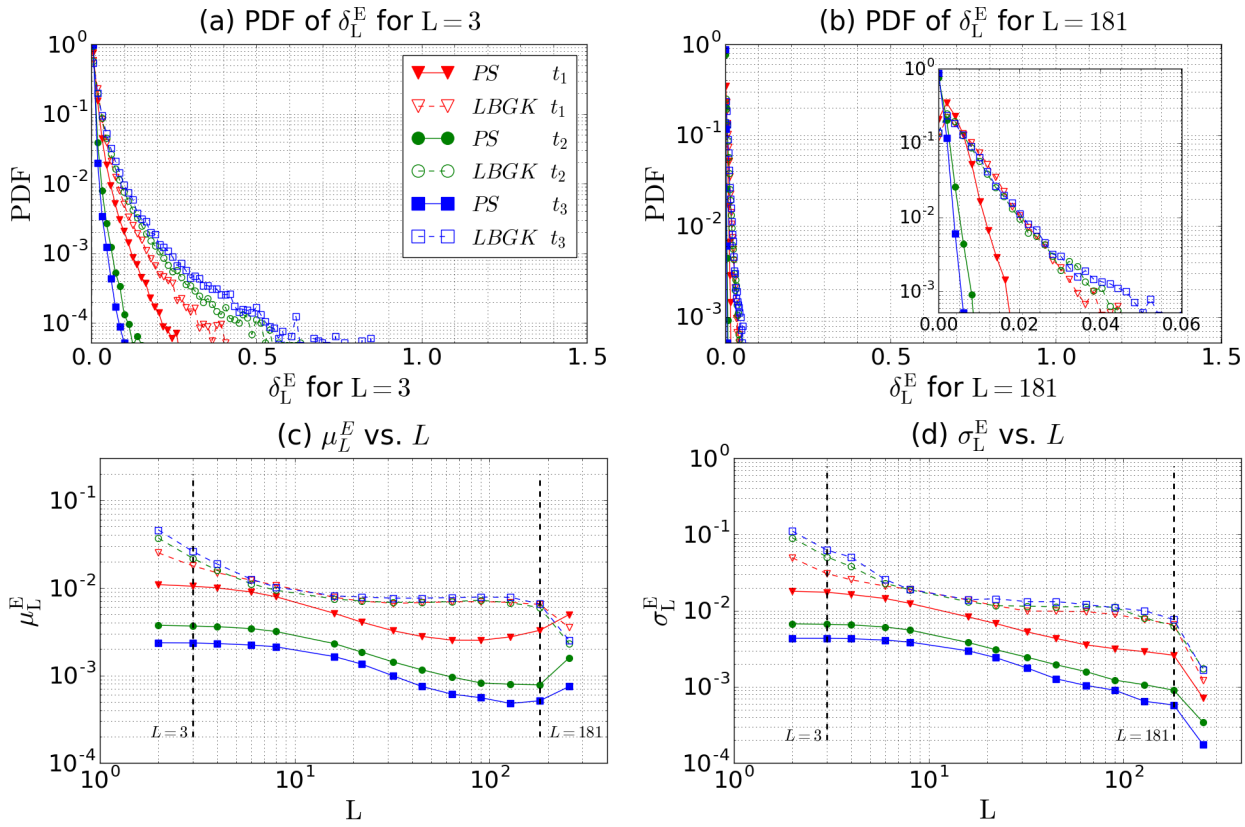

Figure 6: Statistics of the balancing error obtained from the kinetic energy balance δ_L^E (see Eq. (12)) against the characteristic length of the sub-volume L shown for the PS and LBGK ensemble of 25 decaying simulations for three selected times. Top figures are PDFs of the balancing error for sub-volumes corresponding to $L = 3$ (Panel (a)) and $L = 181$ (Panel (b)). Bottom figures are the mean (Panel (c)) and the standard deviation (Panel (d)) of the balancing error.

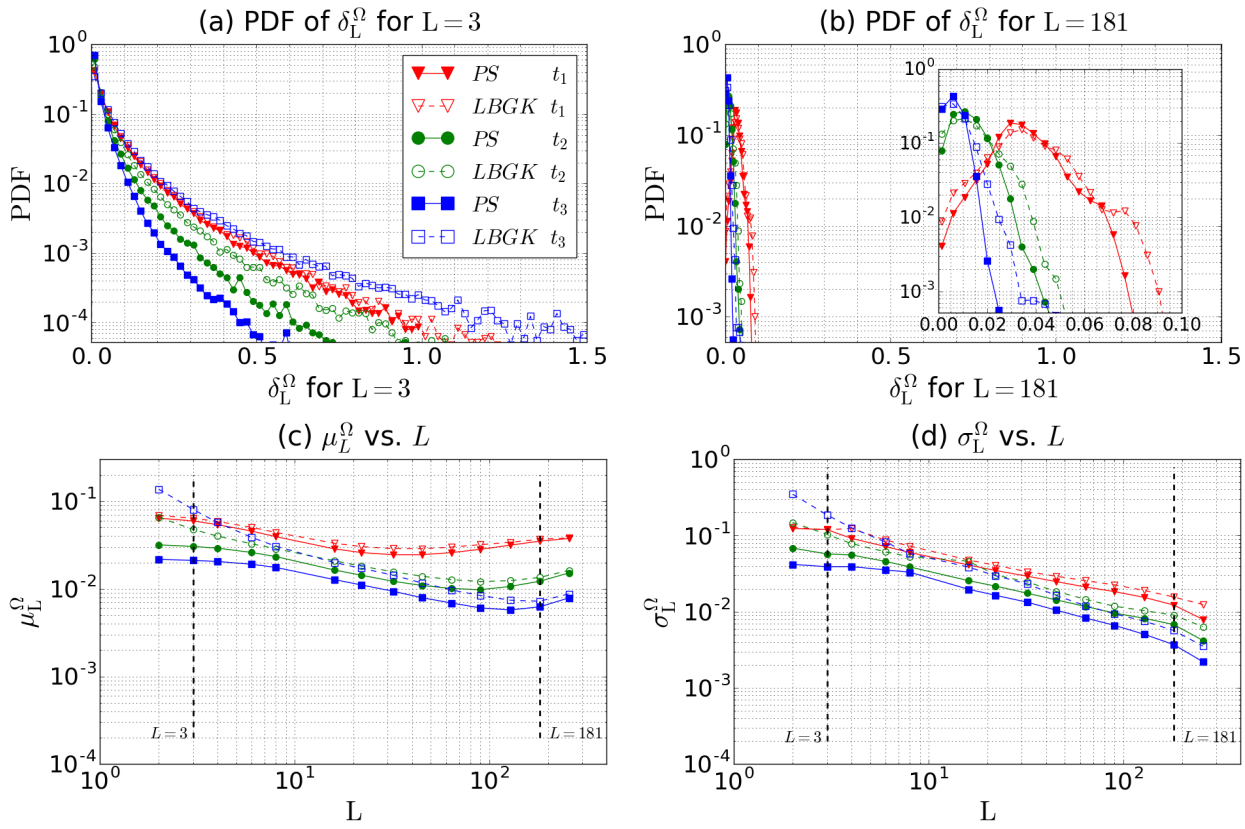

Figure 7: Statistics of the balancing error obtained from the enstrophy balance δ_L^{Ω} (see Eq. (13)) against the characteristic length of the sub-volume L shown for the PS and LBGK ensemble of 25 decaying simulations for three selected times. Top figures are PDFs of the balancing error for sub-volumes corresponding to $L = 3$ (Panel (a)) and $L = 181$ (Panel (b)). Bottom figures are the mean (Panel (c)) and the standard deviation (Panel (d)) of the balancing error.

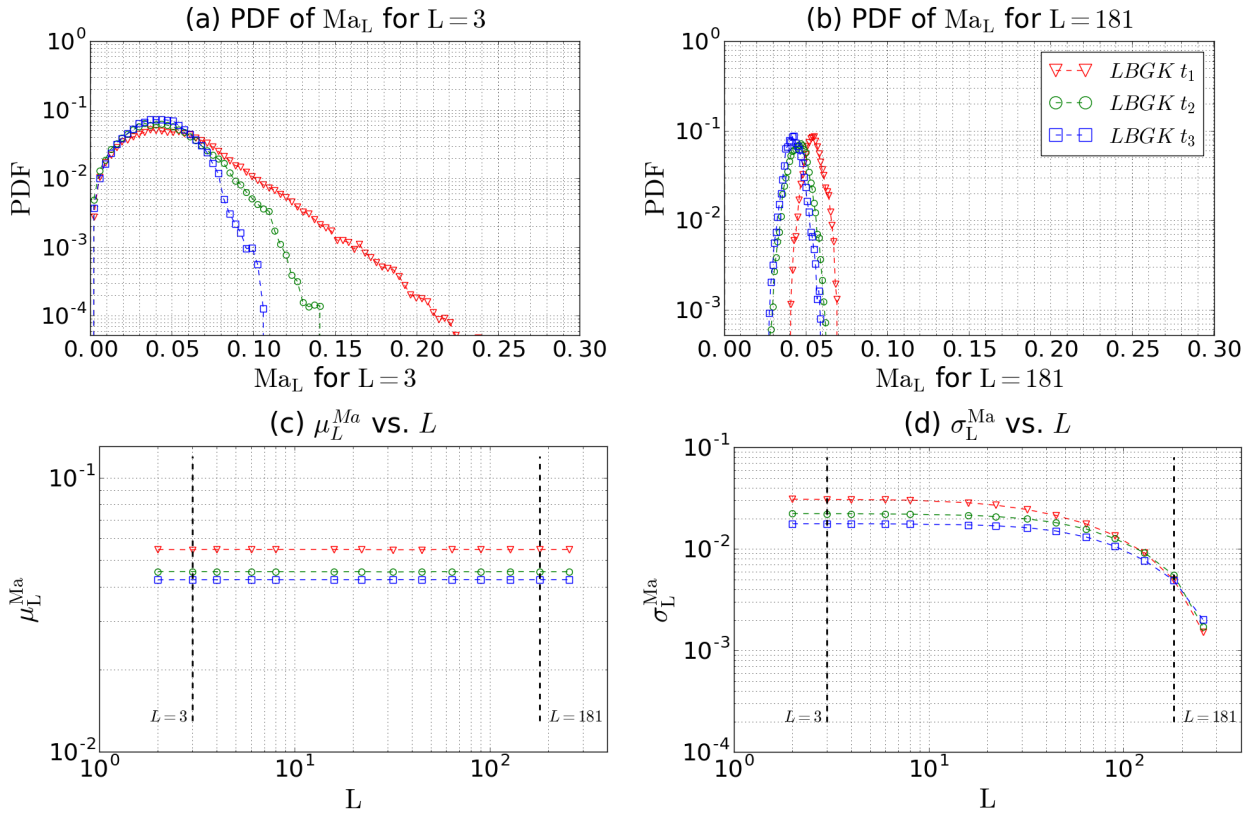

Figure 8: Statistics of the Mach number at scale L (see Eq. (19)) against the characteristic length of the sub-volume L shown for the LBGK ensemble of 25 decaying simulations for three selected times. Top figures are PDF of the balancing error for sub-volumes corresponding to $L = 3$ (Panel (a)) and $L = 181$ (Panel (b)). Bottom figures are the mean (Panel (c)) and the standard deviation (Panel (d)) of Ma_L.

5. Forced LBGK hydrodynamics

Setting up the forcings as described in section 3, we analyze configurations of statistically stationary simulations for five different relaxation times $\tau_0 = 0.60, 0.54, 0.53, 0.52$ and $\tau_0^{last} = 0.515$ beyond which LBGK is no longer stable. We then obtain statistics of the balancing errors by averaging both in space and in time on 25 different configurations (see Fig. 9). We show in Fig. 10 the superposed time-averaged spectrum for the conducted simulations. At large scale, we can see the effect of the energy removal preventing the energy to accumulate and maintaining the large-

scale slope over the backward energy cascade slope of $-\frac{5}{3}$. On the other hand, at small scales, we observe that when we decrease τ_0 (increasing Re) the flow becomes more turbulent and the slope gets increasingly closer to the forward enstrophy cascade slope of -3 [25, 26].

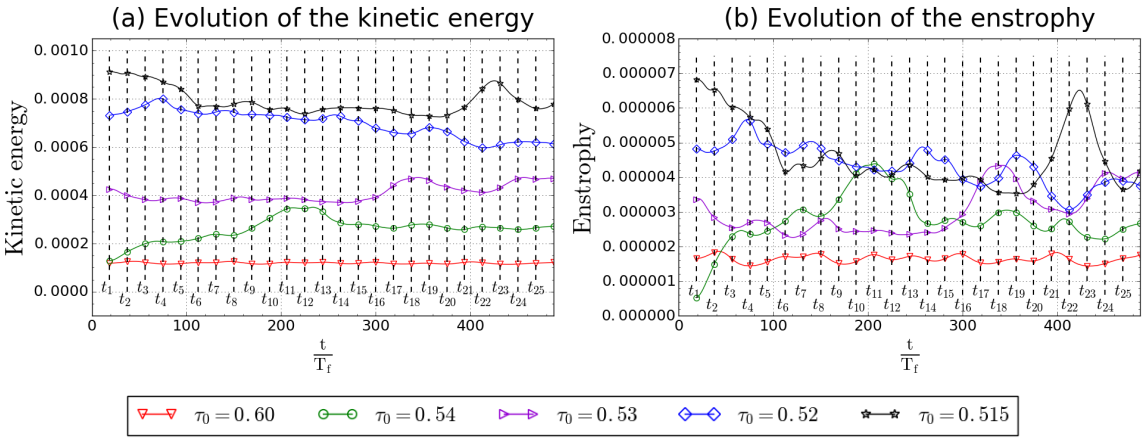

Figure 9: Evolution of the kinetic energy (a) and of the enstrophy (b) of LBGK simulations for five different relaxation times. The 25 vertical lines highlight the time when configurations were processed to gather statistics in space and time of the balancing errors.

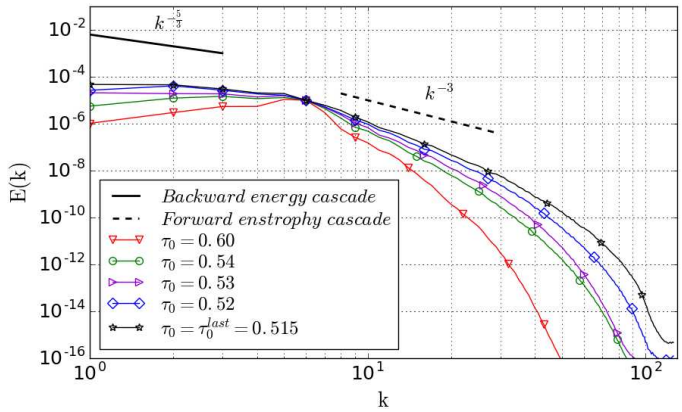

Figure 10: Superposed time-averaged spectrum of LBGK simulations for five different relaxation times.

We present the results of the statistical analysis of the kinetic energy balancing error δ_L^E and

the enstrophy balancing error δ_L^{Ω} in Figs. 11 and 12 respectively. As expected from the LBGK-PS validation results, the hydrodynamic recovery largely depends on the scale of the sub-volume it is measured on. At small scales, we obtain an error that is roughly an order of magnitude larger than at larger scales (see dashed lines in Panels (c)-(d)). For the Reynolds numbers that we have simulated, we observe an inverse dependency on the Reynolds number across scales: while at smaller scales the error decreases with the Reynolds number, this dependence on Reynolds number reverses at $L \approx 10$. Notice, however, that such inverse dependency in the error is only of a few percents, and the corresponding standard deviations are of a few percent as well, hence it is difficult to asses more quantitatively this effect at this stage.

Having forced with fixed forcing amplitudes, the Mach number of the conducted simulations also varies as a function of τ_0. To highlight potential high Mach number effects, we plot again the statistics on the Mach number at scale L, $Ma_L = \left\langle \frac{U_{RMS}}{c_s} \right\rangle_{V=L\times L}$ as shown in Fig. 13. We observe that we are working with Mach number that are qualitatively and quantitatively similar to the ones studied in the previous section (see Fig. 8), hence we conclude again that we work on a range of Mach number that does not impact the hydrodynamics.

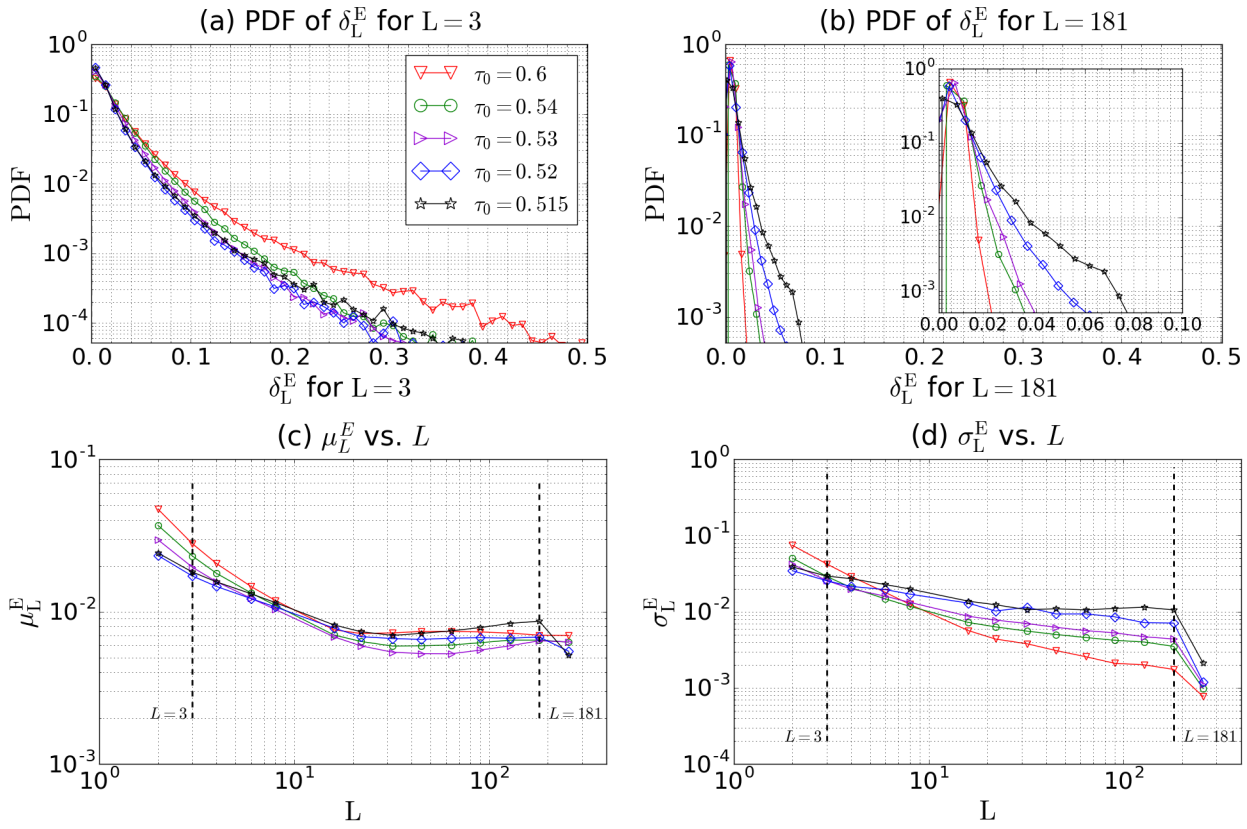

Figure 11: Statistics of the balancing error obtained from the kinetic energy balance δ_L^E (see Eq. (12)) against the characteristic length of the sub-volume L for 5 forced LBGK simulation of different relaxation times. Top figures are PDF of the balancing error for sub-volumes corresponding to $L = 3$ (Panel (a)) and $L = 181$ (Panel (b)). Bottom figures are the mean (Panel (c)) and the standard deviation (Panel (d)) of the balancing error.

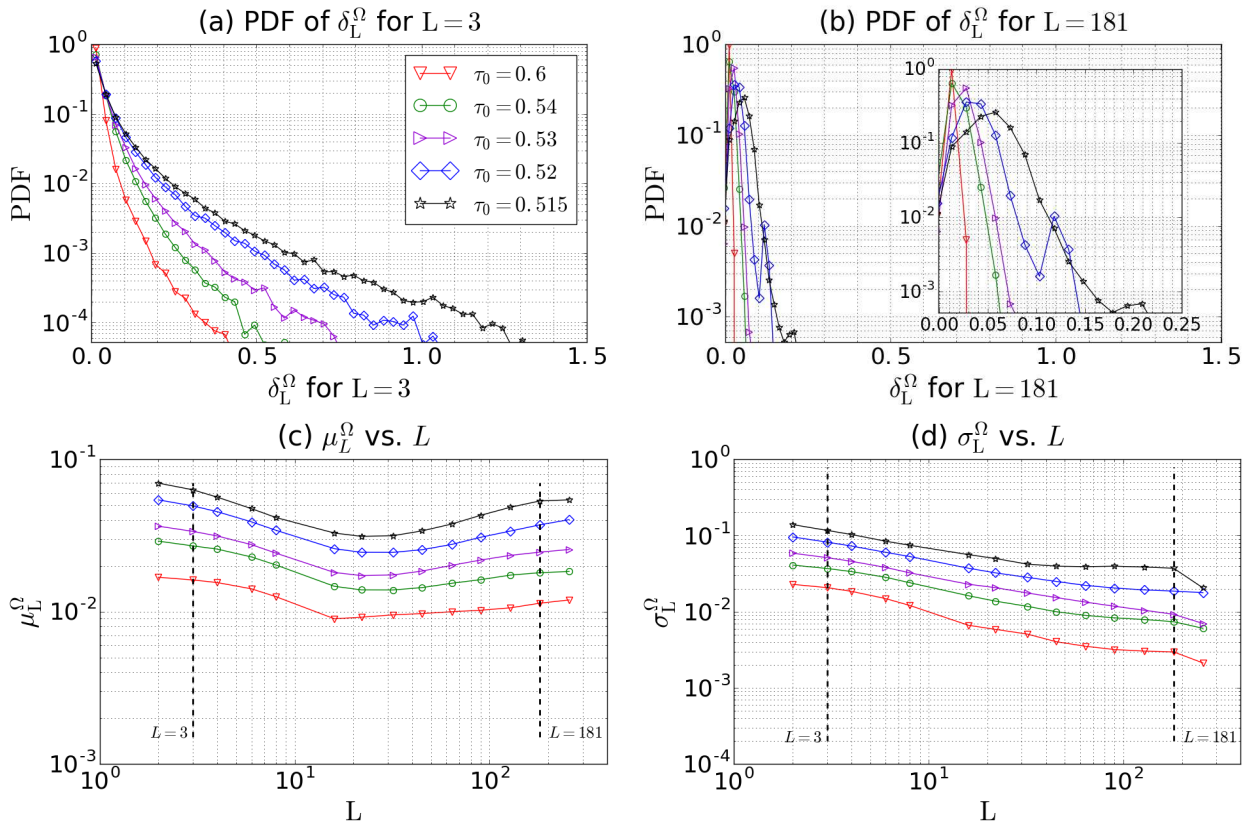

Figure 12: Statistics of the balancing error obtained from the kinetic energy balance δ_L^{Ω} (see Eq. (13)) against the characteristic length of the sub-volume L shown for 5 forced LBGK simulation of different relaxation times. Top figures are PDF of the balancing error for sub-volumes corresponding to $L = 3$ (Panel (a)) and $L = 181$ (Panel (b)). Bottom figures are the mean (Panel (c)) and the standard deviation (Panel (d)) of the balancing error.

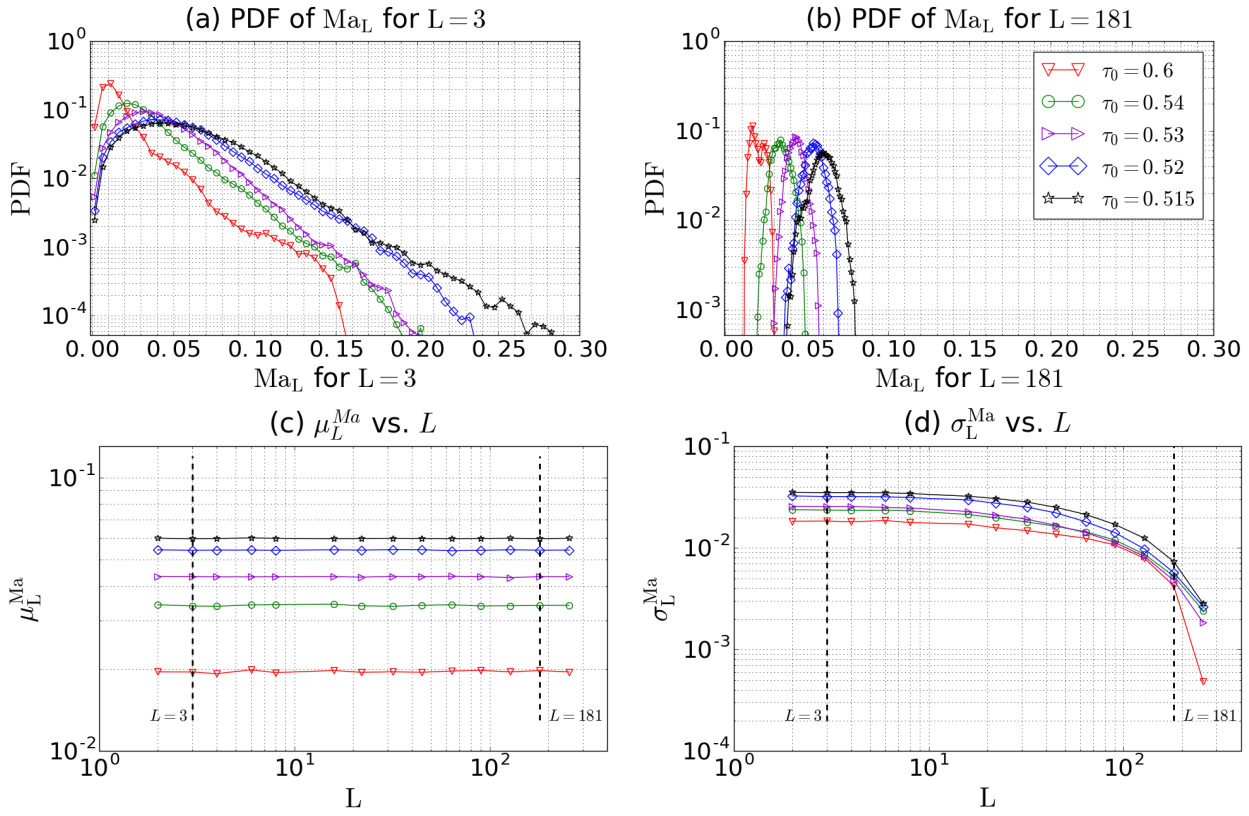

Figure 13: Statistics of the Mach number at scale L (see Eq. (19)) against the characteristic length of the sub-volume L shown for 5 forced LBGK simulation of different relaxation times. Top figures are PDF of the balancing error for sub-volumes corresponding to $L = 3$ (Panel (a)) and $L = 181$ (Panel (b)). Bottom figures are the mean (Panel (c)) and the standard deviation (Panel (d)) of Ma_L.

6. Concluding remarks

We have proposed a general tool to check the generated hydrodynamics of fluid flow simulations. The tool hinges on the calculation of the kinetic energy and the enstrophy balance equation terms averaged over randomly chosen sub-volumes at different scales. We have defined balancing errors, representing the accuracy of the hydrodynamic recovery across scales and conducted a statistical analysis in the context of 2D homogeneous isotropic turbulence. Firstly, we validated this tool on decaying 2D turbulence by systematically comparing an ensemble of LBGK simulations

with an ensemble of PS simulations, both initialized with the same configurations. In all cases, the accuracy of hydrodynamic recovery is non-local and improves at large scales. Moreover, there is one order of magnitude of difference between the balancing errors for energy and enstrophy, which can be explained by the extra discretization error implied by the enstrophy equation, since it involves higher order derivatives than those present in the momentum equation [23]. Secondly, we have applied this tool to check LBGK hydrodynamic in the context of forced 2D turbulence at increasing Reynolds number. All in all, we have observed statistics of the balancing errors both from kinetic energy balance and enstrophy balance that are very similar to the validation LBGK ensemble's results. In both the validation and benchmark, the Mach number was maintained low enough for its effect to be sub-leading in the hydrodynamic recovery.

The ideal continuation of this work is the study of hydrodynamic recovery with LBM in presence of SGS models of eddy viscosity. To this aim, the developed tool is particularly useful, since it allows to quantitatively describe the effects of under-resolution and the possible improvements led by the SGS model.

Acknowledgement

The authors would like to thank Fabio Bonaccorso and Michele Buzzicotti at the University of Rome "Tor Vergata" for their support in conducting the PS simulations. This work was supported by the European Unions Framework Programme for Research and Innovation Horizon 2020 (2014-2020) under the Marie Skłodowska-Curie grant [grant number 642069] and by the European Research Council under the ERC grant [grant number 339032]. It is also part of the research programme CSER with project number 12CS034, which is (partly) financed by the Netherlands Organisation for Scientific Research (NWO).

References

[1] Boris Galperin and Steven A. Orszag. *Large eddy simulation of complex engineering and geophysical flows*. Cambridge University Press, 2010.

[2] Stephen B. Pope. *Turbulent Flows*. Cambridge University press, 2000.

[3] P. A. Davidson. *Turbulence: An Introduction for Scientists and Engineers*. Oxford University Press, 2015.

[4] Heinz Pitsch. Large-Eddy Simulation of Turbulent Combustion. *Annual Review of Fluid Mechanics*, 38(1):453–482, jan 2006.

[5] Claus Albrecht Wagner, Thomas Huttl, and Pierre Sagaut. *Large-eddy simulation for acoustics*. Cambridge University Press, 2007.

[6] Peter P. Sullivan, James C. McWilliams, and Chin-Hoh Moeng. A subgrid-scale model for large-eddy simulation of planetary boundary-layer flows. *Boundary-Layer Meteorology*, 71(3):247–276, nov 1994.

[7] Pierre Sagaut. *Large Eddy Simulation for Incompressible Flows*. Scientific Computation. Springer-Verlag Berlin Heidelberg, 2002.

[8] Sauro Succi. *The Lattice Boltzmann Equation for Fluid Dynamics and Beyond*. Oxford University Press, 2001.

[9] Dieter A. Wolf-Gladrow. *Lattice-Gas Cellular Automata and Lattice Boltzmann Models: An Introduction*. Springer-Verlag Berlin Heidelberg, 2000.

[10] Timm Krüger, Halim Kusumaatmaja, Alexandr Kuzmin, Orest Shardt, Goncalo Silva, and Erlend Magnus Viggen. *The Lattice Boltzmann Method*. Graduate Texts in Physics. Springer International Publishing, Cham, 2017.

[11] P. L. Bhatnagar, E. P. Gross, and M. Krook. A model for collision processes in gases. i. small amplitude processes in charged and neutral one-component systems. *Physical Review*, 94:511–525, May 1954.

[12] Erlend Magnus Viggen. The Lattice Boltzmann Method with Applications in Acoustics. Master's thesis, NTNU, 2009.

[13] Olga Filippova, Sauro Succi, Francesco Mazzocco, Cinzio Arrighetti, Gino Bella, and Dieter Hänel. Multiscale Lattice Boltzmann Schemes with Turbulence Modeling. *Journal of Computational Physics*, 170(2):812–829, jul 2001.

[14] Yu-Hong Dong and Pierre Sagaut. A study of time correlations in lattice Boltzmann-based large-eddy simulation of isotropic turbulence. *Physics of Fluids*, 20(3):035105, mar 2008.

[15] Yu-Hong Dong, Pierre Sagaut, and Simon Marie. Inertial consistent subgrid model for large-eddy simulation based on the lattice Boltzmann method. *Physics of Fluids*, 20(3):035104, mar 2008.

[16] Sheng Chen. A large-eddy-based lattice Boltzmann model for turbulent flow simulation. *Applied Mathematics and Computation*, 215(2):591–598, sep 2009.

[17] Orestis Malaspinas and Pierre Sagaut. Consistent subgrid scale modelling for lattice Boltzmann methods. *Journal of Fluid Mechanics*, 700:514–542, jun 2012.

[18] Kannan N. Premnath, Martin J. Pattison, and Sanjoy Banerjee. Dynamic subgrid scale modeling of turbulent flows using lattice-Boltzmann method. *Physica A: Statistical Mechanics and its Applications*, 388(13):2640–2658, jul 2009.

[19] Bruce M Boghosian, Jeffrey Yepez, Peter V Coveney, and Alexander Wager. Entropic lattice boltzmann methods. *Proceedings of the Royal Society of London A: Mathematical, Physical and Engineering Sciences*,

457(2007):717–766, 2001.

[20] Iliya V. Karlin, Antonio Ferrante, and Hans Christian Öttinger. Perfect entropy functions of the Lattice Boltzmann method. *Europhysics Letters (EPL)*, 47(2):182–188, 1999.

[21] Orestis Malaspinas, Michel Deville, and Bastien Chopard. Towards a physical interpretation of the entropic lattice Boltzmann method. *Physical Review E*, 78(6):066705, dec 2008.

[22] J. Smagorinsky. General circulation experiments with the primitive equations. *Monthly Weather Review*, 91(3):99–194, 1963.

[23] L Biferale, F Mantovani, M Sbragaglia, A Scagliarini, F Toschi, and R Tripiccione. High resolution numerical study of Rayleigh-Taylor turbulence using a thermal lattice Boltzmann scheme. *Physics of Fluids*, 22(115112):1–13, 2010.

[24] A. L. Kuperstokh. New method of incorporating a body force term into the lattice Boltzmann equation. In *Proeedings of the 5th International EDH Workshop*, pages 241–246, Poitiers, France, 2004.

[25] Guido Boffetta and Robert E. Ecke. Two-Dimensional Turbulence. *Annual Review of Fluid Mechanics*, 44(1):427–451, jan 2012.

[26] Uriel Frisch. *Turbulence : the legacy of A.N. Kolmogorov*. Cambridge University Press, 1995.